Research in Astronomy and Astrophysics, 22:125011 (11pp), 2022 December https://doi.org/10.1088/1674-4527/ac9d27

New Continuum and Polarization Observations of the Cygnus Loop with FAST. II. Images and Analyses

Xiao-Hui Sun[1], Xu-Yang Gao[2,3], Wolfgang Reich[4], Peng Jiang[2,3], Di Li[2,3], Huirong Yan[5,6], and Xiang-Hua Li[1]
[1] School of Physics and Astronomy, Yunnan University, Kunming 650500, China; xhsun@ynu.edu.cn, xhli@ynu.edu.cn
[2] National Astronomical Observatories, Chinese Academy of Sciences, Beijing 100101, China; xygao@nao.cas.cn
[3] CAS Key Laboratory of FAST, National Astronomical Observatories, Chinese Academy of Sciences, Beijing 100101, China
[4] Max-Planck-Institut für Radioastronomie, Auf dem Hügel, 53121 Bonn, Germany
[5] Institut für Physik und Astronomie, Universität Potsdam, Haus 28, Karl-Liebknecht-Str. 24/25, D-14476 Potsdam, Germany
[6] Deutsches Elektronen-Synchrotron DESY, Platanenallee 6, D-15738 Zeuthen, Germany

Received 2022 August 23; revised 2022 October 18; accepted 2022 October 22; published 2022 November 16

Abstract

We present total-intensity and polarized-intensity images of the Cygnus Loop supernova remnant (SNR) observed by the Five-hundred-meter Aperture Spherical radio Telescope. The high angular-resolution and high-sensitivity images enable us to thoroughly compare the properties of the northern part with the southern part of the SNR. The central filament in the northern part and the southern part have a similar foreground rotation measure, meaning their distances are likely similar. The polarization analysis indicates that the random magnetic field is larger than the regular field in the northern part, but negligible in the southern part. The total-intensity image is decomposed into components of various angular scales, and the brightness-temperature spectral index of the shell structures in the northern part is similar to that in the southern part in the component images. All the evidence suggests that the northern and southern parts of the Cygnus Loop are situated and thus evolved in different environments of interstellar medium, while belonging to the same SNR.

Key words: ISM: supernova remnants – ISM: magnetic fields – polarization – techniques: polarimetric

1. Introduction

The Cygnus Loop (G74.0−8.5) is a prominent supernova remnant (SNR), which has been observed across a broad electromagnetic spectrum from radio to γ-rays. However, there is no consensus yet on the interpretation and physical nature of the Cygnus Loop. Particularly, the question on whether the southern part is a blowout region from the larger northern part or a separate SNR remains unclear (Uyanıker et al. 2002; Fesen et al. 2018).

In the optical band, the Cygnus Loop clearly exhibits a Balmer Hα shell delineating the boundary of the SNR (Levenson et al. 1998). This thin shell traces the non-radiative shock front at a velocity close to 400 km s^{-1} (Fesen et al. 2018), implying that the SNR is at the early stage of the adiabatic phase. The soft X-ray emission appears to be confined by the Balmer shell, but only fills the interior of the northern part of the SNR (Aschenbach & Leahy 1999). Strong [S II] and [O III] lines as well as UV emission were detected toward the northeastern and the western parts of the SNR, adjacent to the Balmer filament (Levenson et al. 1998; Fesen et al. 2018), which indicates the interaction between shocks and interstellar clouds. Consequently, the shocks are transitioned to be radiative at a velocity around 100 km s^{-1} (Fesen et al. 2018).

In the radio band, the Cygnus Loop is composed of two overlapping shell structures with centers aligned roughly in the north–south direction (Uyanıker et al. 2004a). The northern radio shell well corresponds to the optical emission toward the northeast and the west of the SNR. The strong radio emission from the southern shell, however, has no correspondence in other wavelengths. The two shells share a similar total-intensity spectrum (Uyanıker et al. 2004a; Loru et al. 2021). The polarization characteristics of the two shells are totally different, which can be readily interpreted by the scenario of two separate SNRs (Uyanıker et al. 2002; Sun et al. 2006; West et al. 2016).

The two-SNR scenario does not seem to be corroborated by observations at other wavelengths. The X-ray observations by Uchida et al. (2008) indicate that the plasma temperature and the abundances of Ne, Mg and other elements are similar between the northern and southern parts of the Cygnus Loop, which supports that the southern shell is just a blowout region as proposed by Aschenbach & Leahy (1999). Optical observations by Fesen et al. (2018) reveal that the morphology of the southern shell resembles that of a second possible blowout region in the Cygnus Loop. Katsuda et al. (2012) reported the discovery of an X-ray pulsar and a pulsar-wind nebula in the southern part of the SNR, which would prove the southern shell to be an individual SNR. However, Halpern & Gotthelf (2019) identified these sources as a Seyfert galaxy and a cluster of galaxies, respectively, and a pulsar associated with the Cygnus Loop thus remains elusive.

For the blowout scenario, the exact process is uncertain. The simulations by Fang et al. (2017) demonstrated that a supernova explosion in a cavity evacuated by the winds from the progenitor star can reproduce the morphology of the Cygnus Loop. A multi-wavelength analysis by Fesen et al. (2018) suggested that the Cygnus Loop lies in an extended low-density region rather than a wind-driven cavity, and the interaction between the shocks and the interstellar clouds causes the morphology. In contrast, Tenorio-Tagle et al. (1985) proposed that the supernova explosion occurred in a dense molecular cloud in the southern shell, and the northern part of the SNR is the result of a blowout. However, there is no indication of a dense molecular cloud surrounding the southern shell, as can be seen from the multi-wavelength images presented by Fesen et al. (2018). Meyer et al. (2015) put forward an alternative explanation where a massive runaway star shaped the interstellar medium with a bow shock and a supernova explosion afterwards in the shaped region resulted in the morphology.

We conducted new continuum and polarization observations of the Cygnus Loop with the Five-hundred-meter Aperture Spherical radio Telescope (FAST, Nan et al. 2011; Jiang et al. 2020) to investigate the properties of the SNR. In Paper I (Sun et al. 2021), we verified the data processing and demonstrated the exceptional imaging capability of FAST. In this paper, we will present a detailed analysis of the Cygnus Loop. The paper is organized as follows. We describe the observations and results in Section 2, present discussions in Section 3, and summarize the conclusions in Section 4.

2. Observations and Results

We presented the images from the scanning observations in R.A. direction (FAST project code: 2019a-125-C) in Paper I. There are stripes along the scanning directions in those images, which are caused by drifting of the system. In order to eliminate the stripes, we conducted new scanning observations in decl. direction (FAST project code: PT2021_0111), and combined the observations in both directions to produce the final maps.

The data processing was described in Paper I. In summary: (1) radio frequency interference (RFI) and H I line were mitigated; (2) leakage was corrected and the antenna-temperature scale was established according to the injected reference signal; (3) gains for all the beams were derived from the calibrators 3C 138 or 3C 48; (4) gains were applied to the scans; (5) maps were constructed by combining all the scans, and were multiplied by the conversion factors from antenna temperature to main-beam brightness temperature (T_b). These procedures were repeated for each individual frequency and scan direction. The final maps were obtained by combining the maps from the two orthogonal directions with the basket-weaving method by Emerson & Gräve (1988).

After processing all the observations, we obtained frequency cubes of Stokes parameters I, Q, and U containing nearly 30,000 frequency channels. The width of each frequency channel is about 7.63 kHz. We smoothed all the images to a common angular resolution of $4'$.

2.1. Total Intensity

We averaged the frequency cube of I by taking the median values and obtained the total-intensity image centered at about 1.28 GHz, as shown in Figure 1. In comparison with the image in Paper I, most of the scanning effects have been successfully removed. There is strong emission from the northern part of the SNR consisting of the northeastern shell, the central filament, and the western shell, and the southern part of the SNR, which is similar to the previous radio observations (Uyanıker et al. 2004a; Sun et al. 2006). The northern part has a well-defined circular shape with the geometric center roughly at ($20^{h}51^{m}36^{s}$, $31°03'$), marked as a plus sign in Figure 1.

The rms noise measured from the map is about 16 mK T_b, lower than the value of 20 mK T_b obtained from the map with only R.A. scans presented in Paper I. As discussed in Paper I, this rms noise is also much lower than the confusion level of about 34 mK T_b estimated following Condon (1974) and Meyers et al. (2017), which seems to be an overestimate. However, the current value is consistent with the result published by Uyanıker et al. (1999).

2.2. Polarization

We applied the rotation measure (RM) synthesis (Brentjens & de Bruyn 2005) and RM clean (Heald 2009) to the frequency cubes of Q and U to obtain Faraday depth (ϕ) cubes of complex polarized intensity, defined as Faraday dispersion function $F(\phi)$. The details of the process refer to Paper I. We then searched for peaks in $|F(\phi)|$ toward each individual pixel of the maps. The peak value of $|F(\phi)|$ and the peak location ϕ correspond to the polarized intensity and RM, respectively. Note that RM in rad m^{-2} can be related to thermal electron density n_e in cm^{-3} and line-of-sight magnetic field $B_{\|}$ in μG as,

$$\mathrm{RM} = 0.81 \int_{\mathrm{source}}^{\mathrm{observer}} n_e B_{\|} dl \qquad (1)$$

where dl is the increment of path length along line of sight in units of pc.

We show the polarized-intensity map in Figure 2 (top panel). We also calculated polarized intensity directly from the averaged Q and U as $PI = \sqrt{Q^2 + U^2}$, and the result is also shown in Figure 2 (bottom panel). The two areas centered at about R.A. = $20^{h}54^{m}$, decl. = $28\overset{\circ}{.}5$ and R.A. = $20^{h}46^{m}$, decl. = $30\overset{\circ}{.}2$ with damaged data are marked as blank. As can be seen from these images, the polarized intensities derived with both methods are nearly identical. For some regions such as the source at the end of the central filament, the polarized intensity

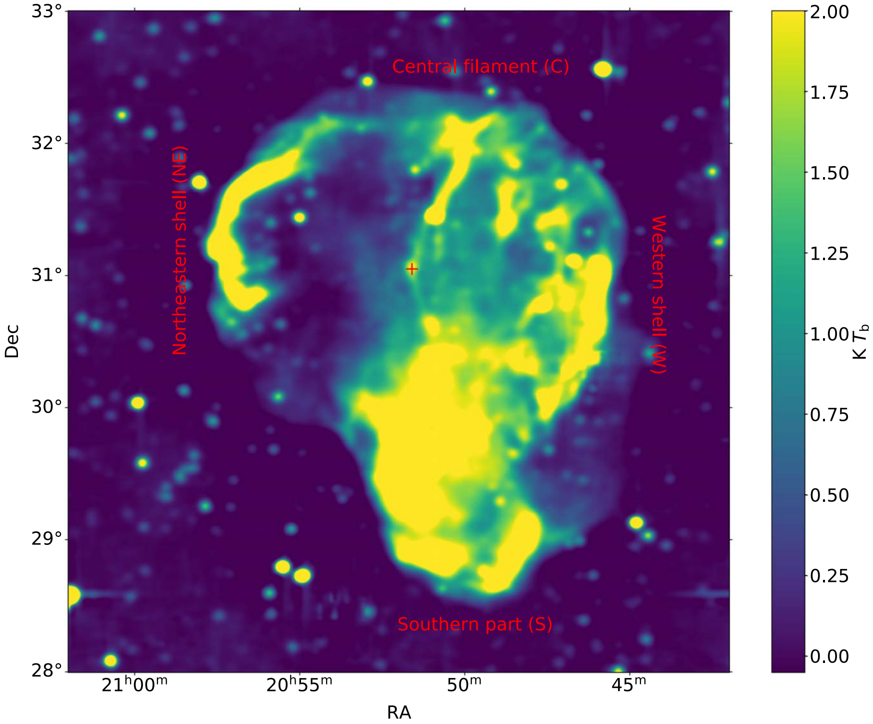

Figure 1. Total-intensity image of the Cygnus Loop from FAST at 1.28 GHz and 4′ angular resolution. The names of some features are marked. The geometric enter of the northern part is marked with a plus sign.

calculated directly from Q and U is much weaker, indicating depolarization after averaging Q and U over all the frequency channels. We therefore used the polarized intensity from RM synthesis for the analysis in below.

The rms noise for polarized intensity is about 4 mK T_b, which is the same as that presented in Paper I. The rms noise does not decrease by adding the decl. scans because of the fluctuations of Galactic diffuse polarized emission. There are several R.A. stripes at decl. of about 28°27′, 29°32′, and 31°42′, which are caused by bad scans.

There is a stark difference for polarization between the northern and southern parts. Toward the north, only the central filament and several fragments from the western shell show polarized emission and the rest is completely depolarized. Toward the south, the polarized emission closely follows the total intensity for the whole area. This is consistent with previous observations presented by Uyanıker et al. (2004a) and Sun et al. (2006).

The RM map is shown in Figure 3. RMs were measured toward the central filament, the southern part and some extragalactic sources, showing strong polarized emission. For the southern part of the SNR, the mean RM is about -16 rad m^{-2} for the lower part and about -20 rad m^{-2} for the upper part, consistent with the value of -21 rad m^{-2} derived by Sun et al. (2006) based on data at 4800 MHz and 2695 MHz. For the central filament, the average RM is about -21 rad m^{-2}, very similar to that of the southern part. Toward all these areas, the RM distribution is very smooth with a standard deviation of about 3 rad m^{-2}.

3. Discussions

3.1. A Multi-wavelength View

We retrieved ROSAT X-ray (Voges et al. 1999) and GALEX near-UV (Bianchi et al. 2017) images from SkyView,[7] and combined them with the FAST radio data into RGB images shown in Figure 4. Here the near-UV data are in red, the radio total intensity and polarization data are in green, and the X-ray data are in blue. Emission visible in all the three bands will appear in white. Similar RGB images have been presented by Uyanıker et al. (2004b) and West et al. (2016) to compare the emission at different wavelengths.

The morphology of the Cygnus Loop in the three bands exhibits clear discrepancy. The X-ray emission is distributed across the entire northern part, with enhancements toward the edges outlining the boundary of the SNR. The near-UV emission is only concentrated on the northeastern shell, the western shell, and the filament in the west of the radio central filament, corresponding to the optically identified bright nebulae (Figure 4): NGC 6992/6995, NGC 6960, and the

---

[7] https://skyview.gsfc.nasa.gov/current/cgi/titlepage.pl

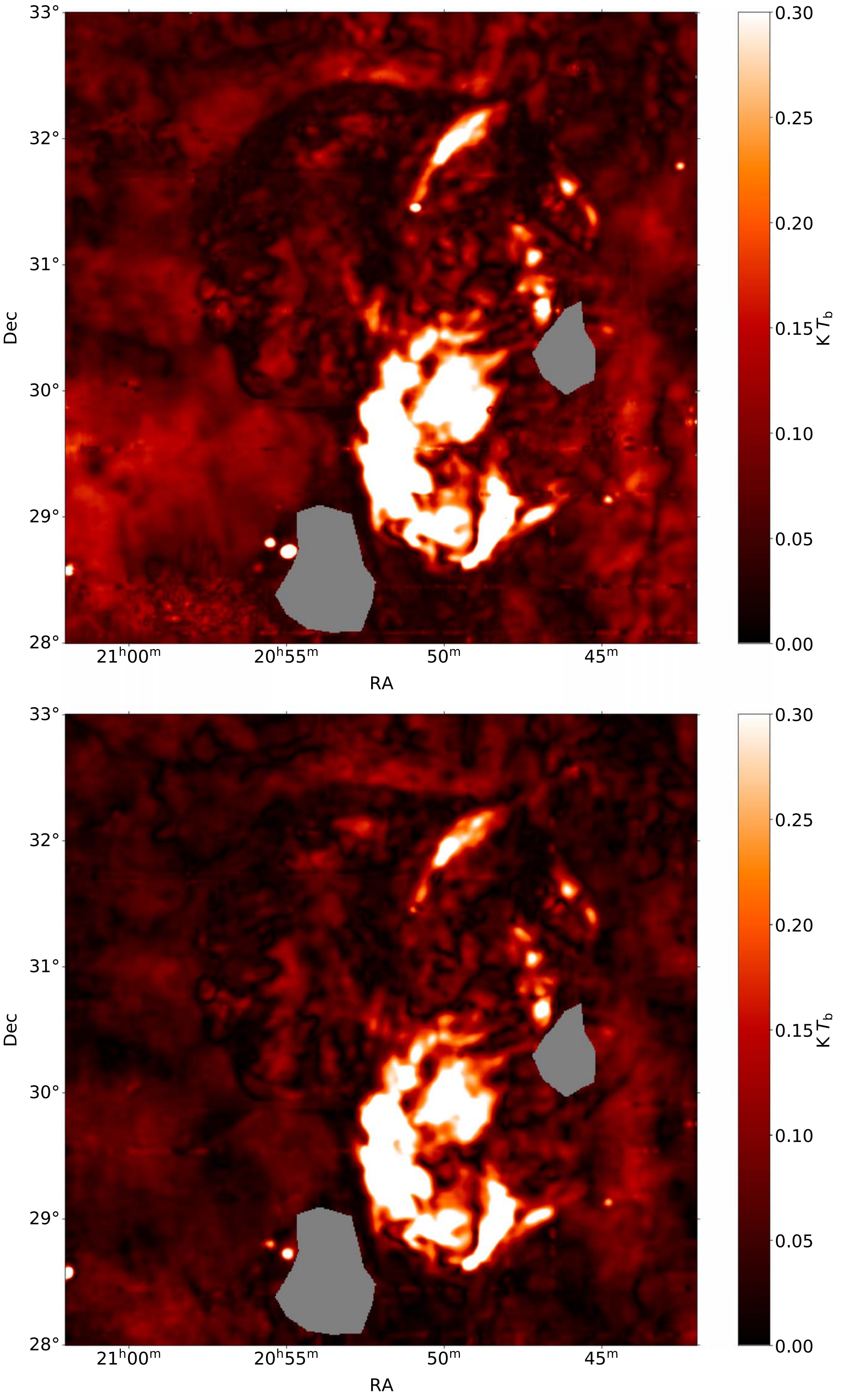

Figure 2. Polarized-intensity images of the Cygnus Loop from FAST at 1.28 GHz, derived from RM synthesis (top panel) and calculated directly from Q and U (bottom panel). The two areas with "damaged" data are marked in gray.

Pickering's triangle (Fesen et al. 2018). Both the X-ray and near-UV emission are confined to the northern part with a weak extension toward the south. The radio total intensity is well correspondent with near-UV and X-ray emission toward the northeastern shell and the western shell. Radio emission dominates the southern part.

The northern part and the southern part of the Cygnus Loop have certainly undergone different paths of evolution, which

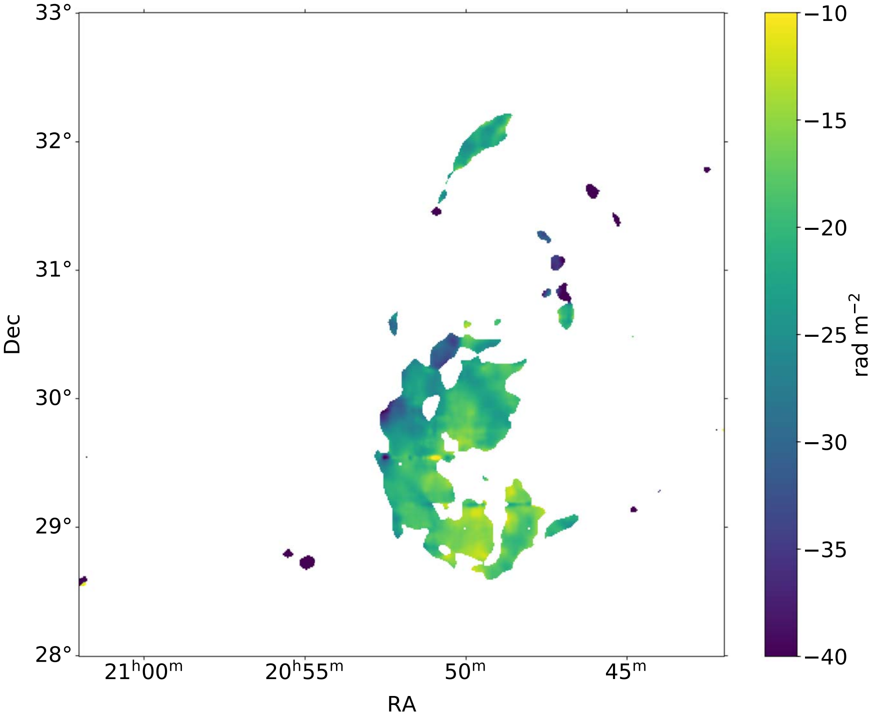

Figure 3. RM map of the Cygnus Loop.

resulted in the different appearance in all the three bands. Toward the north, the strong near-UV emission tracing the interaction between blast wave and dense interstellar clumps (Fesen et al. 2018), is a signature of the SNR entering radiative phase (e.g., Dubner & Giacani 2015). The center-filled X-ray emission is from the swept material or SN ejecta heated by the reverse shock. Toward the south, there is no clear indication of interactions with the ambient medium and the radio morphology resembles a typical SNR in the adiabatic phase.

3.2. RM

RM consists of foreground contribution from the magnetized thermal medium in front of the SNR and the intrinsic contribution from the medium inside the SNR. Toward the central filament and the southern part of the SNR, the degree of polarization, defined as the ratio between the polarized intensity and the total intensity, is similar at 1.4, 2.7, and 4.8 GHz, indicating little depolarization (Sun et al. 2006). This means that the RM contributed by the medium inside the SNR is negligible for these areas, otherwise depolarization toward lower frequencies (1.4 GHz) would be expected.

We can estimate the foreground RM based on Equation (1), RM $\sim 0.81 n_e B_{\|} d$, where d is the distance in pc. Using RMs and dispersion measures of pulsars by Han et al. (2006), the local magnetic field is about 2 μG pointing away from the Sun toward the Cygnus Loop. Based on the thermal electron-density model by Yao et al. (2017), the average electron density in the direction of the Cygnus Loop is about 0.015 cm^{-3}. Substituting these values yields an RM of about $-18\,\mathrm{rad\,m}^{-2}$, consist with the RMs obtained for the central filament and the southern part. We also simulated the RM with the 3D emission models of the Milky Way Galaxy by Sun & Reich (2010), and derived an RM of about $-13\,\mathrm{rad\,m}^{-2}$, consistent with the RM of the lower section of the southern part. These estimates confirm that the RMs are mainly from the foreground contribution.

The RMs of the central filament and the southern part of the Cygnus Loop represent the contribution of the foreground medium. These RMs are consistent with each other within the errors given the scattering of about $3\,\mathrm{rad\,m}^{-2}$. Therefore the similar RM values suggest that these areas should likely be located at the similar distance.

3.3. Depolarization

The bright northeastern shell and the western shell in total intensity (Figure 1) do not have correspondence in polarized intensity (Figure 2). However, polarized emission from these two areas was detected at both 2.7 GHz and 4.8 GHz (Sun et al. 2006), implying a complete depolarization at 1.4 GHz. The low-polarization area extends from the northeastern shell and forms a circular region with a sharp boundary, as can be seen

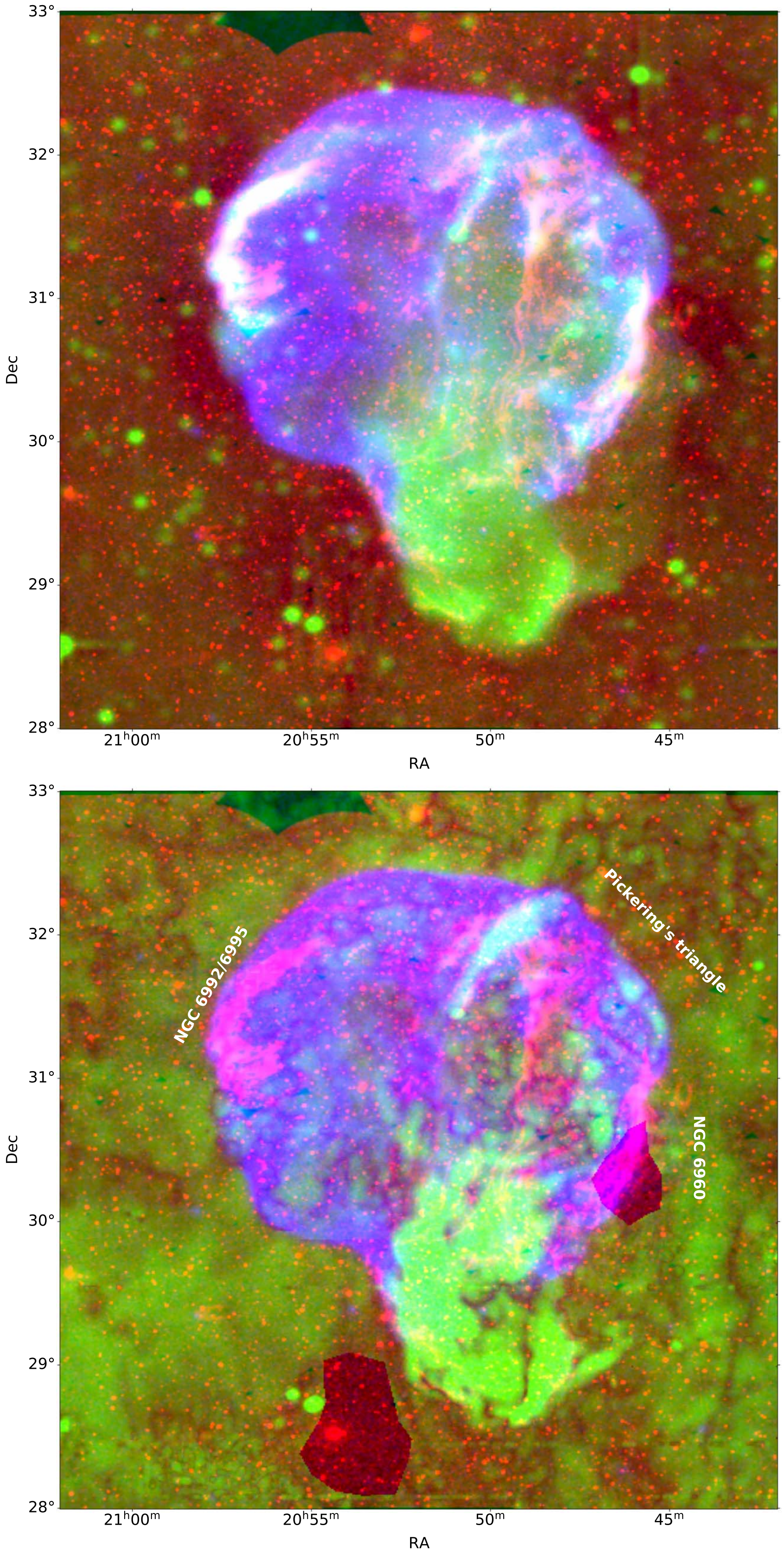

Figure 4. RGB images of the Cygnus Loop. Red: GALEX near-UV. Green: FAST total intensity (top panel) and polarized intensity (bottom panel). Blue: ROSAT X-ray.

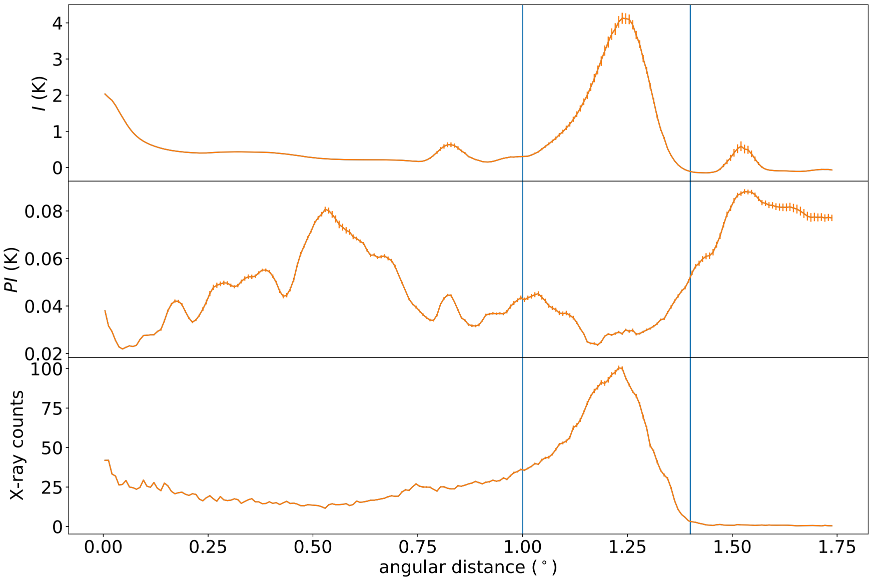

Figure 5. Radio total intensity (*I*), radio polarized intensity (*PI*), and X-ray intensity vs. angular distance from the reference position ($20^{\rm h}51^{\rm m}36^{\rm s}$, $31°03'$) for the northeastern shell. The vertical lines indicate a radius of 1° and $1\overset{\circ}{.}4$, respectively.

from Figure 2. Beyond the boundary, there are extended patches with low-level polarized emission that is not related with the Cygnus Loop.

There are mainly two types of mechanisms that can cause depolarization: depth depolarization and beam depolarization (Sokoloff et al. 1998). For depth polarization, the synchrotron-emitting and Faraday-rotating medium coexist, so that polarization from different locations along the line of sight experiences different Faraday rotation. Thus adding these emission components partly or completely cancels the polarization. For beam depolarization, the Faraday-rotating medium is in front of the synchrotron-emitting medium. Because of the RM fluctuation, the polarized emission varies across the beam. Averaging the emission within the beam also reduces the polarization following $\Pi = \Pi_0 \exp(-2\sigma_{\rm RM}^2 \lambda^4)$, where Π and Π_0 are observed and intrinsic degree of polarization, $\sigma_{\rm RM}$ is the dispersion of RMs, and λ is the wavelength. Beam depolarization is the primary cause of the mottled structures in polarization images (e.g., Sun et al. 2014), and has been found to account for depolarization toward repeating fast radio bursts (Feng et al. 2022).

In Figure 5, we show the profiles of radio total and polarized, and X-ray intensities vs. angular distance from the reference position ($20^{\rm h}51^{\rm m}36^{\rm s}$, $31°03'$) which is approximately the geometric center of the northern part of the Cygnus Loop (Figure 1). The profiles were derived toward the northeastern shell. The radii of 1° and $1\overset{\circ}{.}4$ are also marked in Figure 5. Within this annulus of about $0\overset{\circ}{.}4$, both radio total and X-ray intensities are high, but the polarized intensity is low. Outside the radius of $1\overset{\circ}{.}4$, there are virtually no radio total and X-ray intensities, but there is considerable amount of polarization that originates from the interstellar medium of the Galaxy rather than from the Cygnus Loop.

The polarization patches adjacent to the Cygnus Loop (Figure 2), which cause the increase of polarized intensity beyond the radius of $1\overset{\circ}{.}4$ (Figure 5), imply that the Galactic polarized emission behind the Cygnus Loop is smeared out. This favors the beam depolarization as the cause of disappearance of polarization toward the northeastern and western shell. The beam depolarization results in mottled polarization structures which are also prevalent across the SNRs. The ratio of the degree of polarization between 2.7 and 4.8 GHz is about 80% (Sun et al. 2006), meaning the RM fluctuation is about $\sigma_{\rm RM} \sim 30$ rad m^{-2}. This amount of RM fluctuation is sufficient to cause complete depolarization at 1.4 GHz.

From the composite Hα all-sky map (Finkbeiner 2003), the Hα intensity ($I_{{\rm H}\alpha}$) is about 30 Rayleigh toward the northeastern shell, where only low angular-resolution (∼1°) data from Wisconsin Hα Mapper (Haffner et al. 2003) are available. Following Haffner et al. (1998) and neglecting absorption, the emission measure (EM) can be derived as EM $= 2.75 T_4^{0.9} I_{{\rm H}\alpha}$. Here EM is in pc cm^{-6}, the electron temperature T_4 is in 10^4 K, and $I_{{\rm H}\alpha}$ is in Rayleigh. Taking $I_{{\rm H}\alpha}$ of 30 Rayleigh and the typical value of $T_4 = 0.8$, we obtained an EM of 67.5 pc cm^{-6}. The brightness temperature contributed by the thermal gas of temperature $T = 8000$ K at frequency $\nu = 1.28$ GHz can be estimated as $8.235 \times 10^{-2} T^{-0.35} \nu^{-2.1} {\rm EM} \approx 0.1$ K (e.g., Sun et al. 2011), which only takes up several percent of the total intensity. The radio emission at 1.28 GHz is predominately from synchrotron emission.

We used the distance of 725 ± 15 pc for the Cygnus Loop, which was derived from the parallaxes of the stars associated

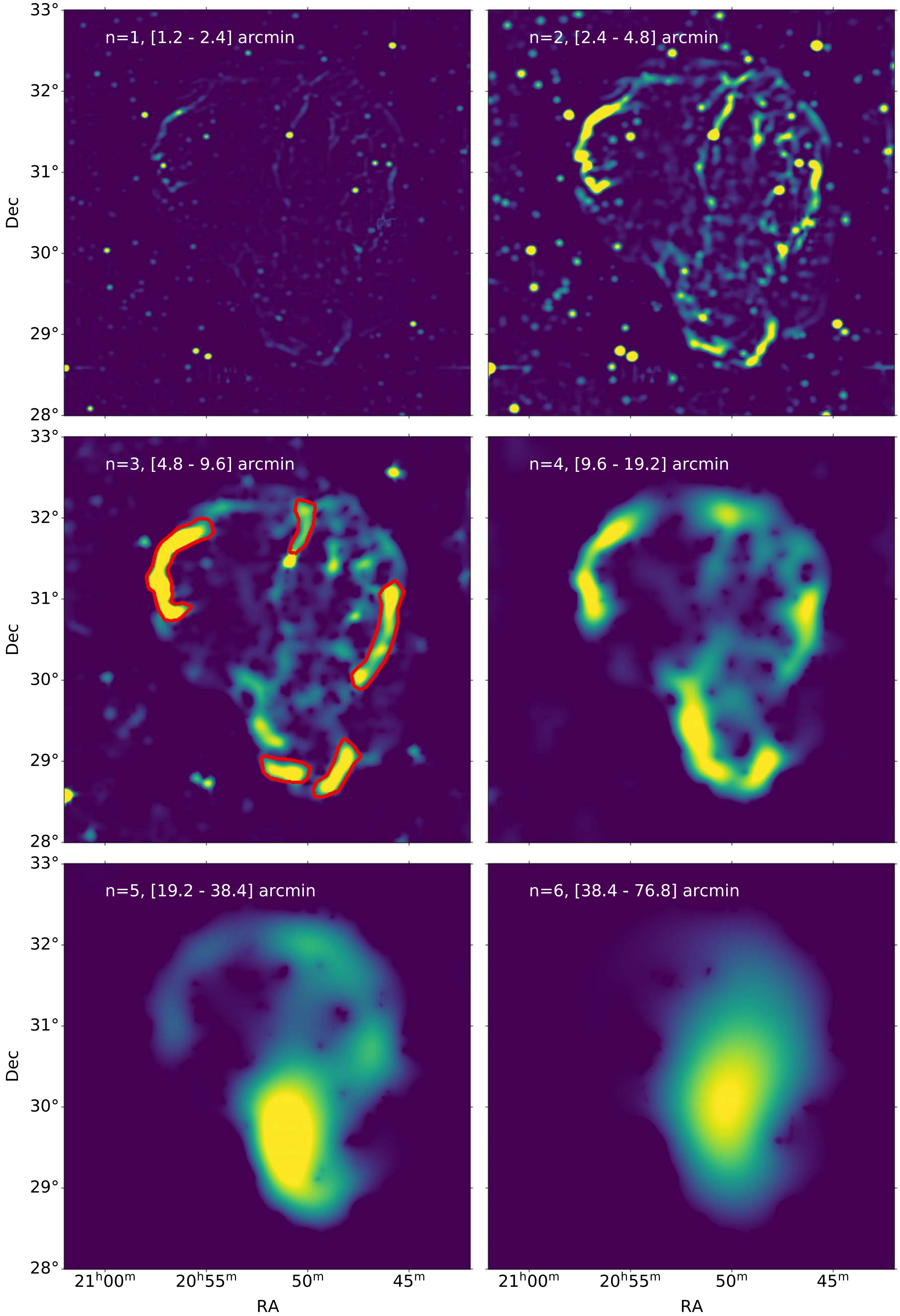

Figure 6. Component images from the constrained diffusion decomposition (CDD) of the Cygnus Loop. The component number *n* and the corresponding range of the angular scales are marked in each panel. The areas used for TT-plots are outlined by red polygons. The color scale extends from 0 (dark) to 0.8 K T_b (bright).

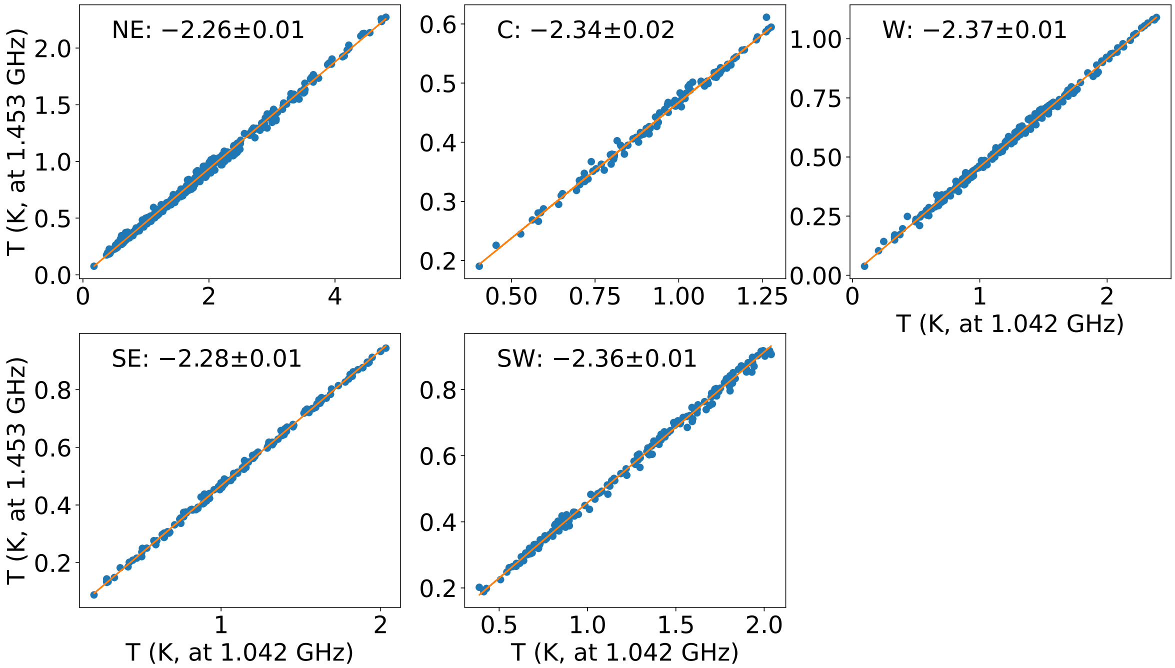

Figure 7. TT-plots for the shell structures in component $n = 3$.

with the SNR (Fesen et al. 2021). The width of the northeastern shell is about $0\overset{\circ}{.}4$ (Figure 5), corresponding to a size of 5 pc. Assuming a spherical shell, the path length along line of sight, L, is thus about 25 pc.

Toward the northeastern shell, the thermal electron density n_e can be derived according to EM $\sim n_e^2 L$, which is about 1.6 cm^{-3}. Here the volume filling factor for the thermal electrons is assumed to be 1. The RM fluctuation can be represented as $\sigma_{\rm RM} \sim 0.81 n_e b \sqrt{Ll}$ (e.g., Sun et al. 2011), where b represents the strength of random magnetic field in μG, and l is the correlation scale for magnetic field fluctuations in pc. For beam depolarization, l should be much smaller than the beamwidth of $4'$ or 0.8 pc. Therefore the lower limit of b is about 5 μG. Toward the western shell, where the Hα data are from the high angular resolution ($\sim$1$'$) Virginia Tech Spectral line Survey (Dennison et al. 1998), the Hα intensity is in the range of 50–140 Rayleigh, corresponding to EM of 112.5–315.0 pc cm^{-6}, and electron density of 2.1–3.5 cm^{-3}. This leads to an estimate of the lower limit of b of about 3 μG.

The average RM derived from the data at 4800 MHz and 2695 MHz is about -70 rad m^{-2} toward the northeastern and western shell (Sun et al. 2006). The intrinsic RM is thus about -50 rad m^{-2} after taking into account the foreground contribution of about -20 rad m^{-2}. The strength of the regular magnetic field can then be estimated to be about 1.5 μG, which is smaller than that of the random magnetic fields.

Tutone et al. (2021) modeled the emission of the Cygnus Loop at γ-ray, X-ray, UV and radio bands, and obtained a magnetic field of about 10 μG toward the northeastern part. For the western part, they used a magnetic field about 244 μG derived by Raymond et al. (2020) toward thin optical filaments. Loru et al. (2021) modeled the γ-ray and radio emission and obtained a magnetic field of about 10 μG for the whole SNR. Note that these magnetic fields include both regular and random components. Together with these previous results, our estimate with a regular field of 1.5 μG and a lower limit of 5 μG toward the northeastern part and of 3 μG toward the western part for the random field corroborates that the random field is much larger than the regular field.

Toward the southern part, the Hα intensity is at a similar level to the northeastern shell, but there is nearly no depolarization. This suggests that the magnetic field fluctuation is negligible.

3.4. A Multi-scale Analysis

We decomposed the total-intensity image shown in Figure 1 into components of various angular scales using the constrained diffusion decomposition (CDD) method developed by Li (2022). In contrast with other multi-scale decomposition methods, the CDD method does not produce artifacts containing negative values around extended structures. The component images are shown in Figure 6. For component n, the corresponding scales of the structures are larger than $2^n\Delta$ but smaller than $2^{n+1}\Delta$, where $\Delta = 0\overset{\prime}{.}6$ is the grid size of the map.

Both the northern and southern parts of the Cygnus Loop show bright shell structures predominantly in components $n = 2$ and $n = 3$ (Figure 6). For component $n = 2$, the angular scale is roughly equal to the beam size, and the structures in this component might be susceptible to beam averaging. We will focus on component $n = 3$ in the analyses below. The northern part consists of the northeastern shell (NE), the central filament (C), and the western shell (W); whereas the southern part can be decomposed into two shells at southeast (SE) and southwest (SW), respectively. We outlined these features in Figure 6.

We made temperature versus temperature plots (TT-plots, Turtle et al. 1962) to determine the brightness temperature spectral index β, defined as $T_\nu \propto \nu^\beta$. The flux density spectral index α, defined as $S_\nu \propto \nu^\alpha$ with S_ν being the flux density, can then be obtained as $\alpha = \beta + 2$. We picked up the two frequency channels well apart at 1.042 GHz and 1.453 GHz to derive TT-plots for component $n = 3$, and the results are shown in Figure 7. Note that the features outlined in Figure 6 for component $n = 3$ have a very good correspondence between these two frequencies.

For component $n = 3$ with angular scales from $4.'8$ to $9.'6$, the northern and southern parts of the SNR have very similar spectra. The spectral indices of the northeastern and southeastern shells are both around -2.27, and the spectral indices of the western and southwestern shells are both around -2.36.

3.5. Remarks on the Morphology of the Cygnus Loop

The northern part of the Cygnus Loop has been interacting with dense interstellar clumps, which can be inferred from the multi-wavelength view of the SNR. The interactions can increase the random magnetic field which causes complete depolarization toward the northeastern and western shells at 1.28 GHz. The similarities of foreground RMs and brightness-temperature spectral indices further suggest that these two parts belong to the same SNR.

4. Conclusions

We obtained total-intensity and polarized-intensity maps of the Cygnus Loop by combining observations scanning in R.A. and decl. directions. We also derived an RM map using RM synthesis.

We compared the properties of the northern part with the southern part of the Cygnus Loop in several aspects. From a multi-wavelength view, the interaction with the ambient interstellar clumps caused the northern part to resemble an SNR in the radiative phase, whereas the southern part resembles a typical SNR in the adiabatic phase. The depolarization in the northern part indicates that the random magnetic fields are stronger than the regular fields. In contrast, the random fields are negligible in the southern part. We decomposed the total intensity into components of various angular scales. The TT-plots for the structures in different component maps show that the northern part and the southern part have similar spectra. These suggest that the northern and southern parts belong to the same SNR.

Acknowledgments

X.S. is supported by the Cultivation Project for FAST Scientific Payoff and Research Achievement of CAMS-CAS. X.S. and X.L. are supported by the Science & Technology Department of Yunnan Province—Yunnan University Joint Funding (2019FY003005). X.S. and X.G. are supported by the CAS-NWO cooperation program (Grant No. GJHZ1865). We would like to thank Dr. Guangxing Li for fruitful discussions and Dr. Patricia Reich for careful reading of the manuscript. We also thank the anonymous referee for the comments that help improve the paper.

ORCID iDs

Xiao-Hui Sun https://orcid.org/0000-0002-3464-5128

References

Aschenbach, B., & Leahy, D. A. 1999, A&A, 341, 602
Bianchi, L., Shiao, B., & Thilker, D. 2017, ApJS, 230, 24
Brentjens, M. A., & de Bruyn, A. G. 2005, A&A, 441, 1217
Condon, J. J. 1974, ApJ, 188, 279
Dennison, B., Simonetti, J. H., & Topasna, G. A. 1998, PASA, 15, 147
Dubner, G., & Giacani, E. 2015, A&ARv, 23, 3
Emerson, D. T., & Gräve, R. 1988, A&A, 190, 353
Fang, J., Yu, H., & Zhang, L. 2017, MNRAS, 464, 940
Feng, Y., Li, D., Yang, Y.-P., et al. 2022, Science, 375, 1266
Fesen, R. A., Weil, K. E., Cisneros, I., Blair, W. P., & Raymond, J. C. 2021, MNRAS, 507, 244
Fesen, R. A., Weil, K. E., Cisneros, I. A., Blair, W. P., & Raymond, J. C. 2018, MNRAS, 481, 1786
Finkbeiner, D. P. 2003, ApJS, 146, 407
Haffner, L. M., Reynolds, R. J., & Tufte, S. L. 1998, ApJL, 501, L83
Haffner, L. M., Reynolds, R. J., Tufte, S. L., et al. 2003, ApJS, 149, 405
Halpern, J. P., & Gotthelf, E. V. 2019, ApJ, 882, 155
Han, J. L., Manchester, R. N., Lyne, A. G., Qiao, G. J., & van Straten, W. 2006, ApJ, 642, 868
Heald, G. 2009, in Cosmic Magnetic Fields: From Planets, to Stars and Galaxies, ed. K. G. Strassmeier, A. G. Kosovichev, & J. E. Beckman, Vol. 259 (Cambridge: Cambridge Univ. Press), 591
Jiang, P., Tang, N.-Y., Hou, L.-G., et al. 2020, RAA, 20, 064
Katsuda, S., Tsunemi, H., Mori, K., et al. 2012, ApJL, 754, L7
Levenson, N. A., Graham, J. R., Keller, L. D., & Richter, M. J. 1998, ApJS, 118, 541
Li, G.-X. 2022, ApJS, 259, 59
Loru, S., Pellizzoni, A., Egron, E., et al. 2021, MNRAS, 500, 5177
Meyer, D. M. A., Langer, N., Mackey, J., Velázquez, P. F., & Gusdorf, A. 2015, MNRAS, 450, 3080
Meyers, B. W., Hurley-Walker, N., Hancock, P. J., et al. 2017, PASA, 34, e013
Nan, R., Li, D., Jin, C., et al. 2011, IJMPA, 20, 989
Raymond, J. C., Chilingarian, I. V., Blair, W. P., et al. 2020, ApJ, 894, 108
Sokoloff, D. D., Bykov, A. A., Shukurov, A., et al. 1998, MNRAS, 299, 189
Sun, X. H., Gaensler, B. M., Carretti, E., et al. 2014, MNRAS, 437, 2936
Sun, X.-H., Meng, M.-N., Gao, X.-Y., et al. 2021, RAA, 21, 282
Sun, X.-H., & Reich, W. 2010, RAA, 10, 1287
Sun, X. H., Reich, W., Han, J. L., et al. 2011, A&A, 527, A74
Sun, X. H., Reich, W., Han, J. L., Reich, P., & Wielebinski, R. 2006, A&A, 447, 937
Tenorio-Tagle, G., Rozyczka, M., & Yorke, H. W. 1985, A&A, 148, 52
Turtle, A. J., Pugh, J. F., Kenderdine, S., & Pauliny-Toth, I. I. K. 1962, MNRAS, 124, 297

Tutone, A., Ballet, J., Acero, F., D'Aì, A., & Cusumano, G. 2021, A&A, 656, A139

Uchida, H., Tsunemi, H., Katsuda, S., & Kimura, M. 2008, ApJ, 688, 1102

Uyanıker, B., Fürst, E., Reich, W., Reich, P., & Wielebinski, R. 1999, A&AS, 138, 31

Uyanıker, B., Reich, W., Yar, A., & Fürst, E. 2004a, A&A, 426, 909

Uyanıker, B., Reich, W., Yar, A., Kothes, R., & Fürst, E. 2002, A&A, 389, L61

Uyanıker, B., Reich, W., Yar-Uyanıker, A., Kothes, R., & Fürst, E. 2004b, in The Magnetized Interstellar Medium, ed. B. Uyanıker, W. Reich, & R. Wielebinski, 153

Voges, W., Aschenbach, B., Boller, T., et al. 1999, A&A, 349, 389

West, J., Safi-Harb, S., Reichardt, I., et al. 2016, Supernova Remnants: An Odyssey in Space after Stellar Death, 35

Yao, J. M., Manchester, R. N., & Wang, N. 2017, ApJ, 835, 29